

Technical Note

Single-phase flow in a rock fracture: micro-model experiments and network flow simulation

J.-T. Cheng^a, J.P. Morris^{a,1}, J. Tran^b, A. Lumsdaine^c, N.J. Giordano^a,
D.D. Nolte^a, L.J. Pyrak-Nolte^{a,d,*}

^a Department of Physics, 1396 Physics Building, 525 Northwestern Avenue, Purdue University, West Lafayette, IN 47907-2036, USA

^b Information Sciences Institute, 4676 Admiralty Way, Suite 1001, Marina del Rey, CA 90292, USA

^c Computer Science Department, Indiana University, 215 Lindley Hall, Bloomington, IN 47405, USA

^d Department of Earth & Atmospheric Science, 550 Stadium Mall Drive., Purdue University, West Lafayette, IN 47907-2051, USA

Accepted 1 January 2004

1. Introduction

Studies of micro-models of porous media have yielded much insight into fluid flow in a wide variety of systems. Micro-models enable the investigation of the fundamental physics of fluid flow in two-dimensional porous systems. While flow in rock occurs in three dimensions through a connected network of pores, cracks and fractures, micro-models can provide insight into specific issues connected with flow in a porous medium. Micro-models can be tailored to a desired geometry, size, pore structure or fracture channel, so that a particular effect can be clearly isolated and studied. Micro-models can be designed to permit measurements, such as direct optical visualization, which are not possible in rock and soil. Both of these features have been used quite successfully in previous work with fluid micro-models.

Micro-models have been used by several investigators to study fluid flow in various geometries [1–8]. These models contain pore structures that permit the flow of one or more fluids to be studied, and can be designed to study the role of a single continuously varying parameter such as porosity. Previous work on micro-models has focused on the geometrical aspects of the flow, including studies of the geometry of invading fronts, pressure-saturation relationships, and percola-

tion-related issues. The measurement of absolute flow rates, and their relation to the micro-model geometry is a much more difficult problem. In this technical note, we present the results of an investigation to compare flow measurements through micro-models to numerical calculations of absolute flow. This study investigates the flow properties of single fractures of constant aperture and variable contact area using synthetic micro-models and a network flow model.

2. Micro-models

The micro-models used in this study were fabricated using projection photolithography to produce voids with known geometry. Previous studies have used the openings in the photo-sensitive layer as an etching mask [5–8]. In contrast to the previous work, we use the photo-sensitive layer itself to accommodate the voids to take advantage of the high spatial resolution and vertical side walls. This approach produces channels with better dimensional control (size and shape) and straighter side walls [1–4]. In previous work the spatial resolution of the voids typically ranged from 100 μm to 1 mm. In our study, 2 μm resolution has been achieved by using a thinner photoresist (Type AZ photoresist) which allows much better spatial resolution and control, thereby permitting the production of voids with sub-micron lateral dimensions [9,10]. Because Type AZ photoresist is used in high-resolution microlithography (for producing integrated circuits) its properties are well known and make it possible to produce micro-models with precise distributions of contact area.

*Corresponding author. Department of Physics, 1396 Physics Building, 525 Northwestern Avenue, Purdue University, West Lafayette, IN 47907-2036, USA. Tel.: +1-765-494-3027; fax: +1-765-494-0706.

E-mail address: ljpn@physics.purdue.edu (L.J. Pyrak-Nolte).

¹ Geophysics and Global Security Division, Lawrence Livermore National Laboratory, P.O. Box 808, L-206, Livermore, CA 94551-9900, USA.

3. Sample preparation

Shipley-type AZ photoresist [11] was applied to a substrate (microscope cover glasses cleaned in ethanol, Fig. 1) by adding drops of photoresist onto the substrate while it was rotating at 5000 rpm (a process known as spinning). This produced an even layer of photoresist with a thickness of 1.06 μm . The thickness of the photoresist layer depends on the viscosity of the photoresist and the spin rate. By using photoresist with different viscosities the thickness of the layer can be varied from 0.5 to 2.7 μm . This thickness controlled the depth of the voids of the final micro-model. After spin coating the glass substrate with photoresist, the sample was baked in air at 100°C for 5 min to remove excess solvent.

The desired computer-generated pattern was transferred into the photoresist by exposing it to light through an optical mask. In this study, two methods were used to transfer patterns to the photoresist: contact printing and projection printing. In the first method a mask which contained a negative image of the desired pattern was made. The mask was transparent to light in the void regions and opaque elsewhere. The mask was placed in direct contact with the photoresist layer, and

the photoresist was exposed to light through the mask. In the exposed regions the photoresist became soluble to a developer solution (a buffered base). After a brief time in this solution the exposed photoresist dissolved while the unexposed photoresist remained on the substrate.

This direct one-to-one exposure is straightforward. However, more precise control over the micro-model geometry can be achieved by projecting a mask image through an optical microscope onto the photoresist [12]. This demagnifies the mask pattern, relaxing the dimensional requirements for the mask. In our study a 5×5 or $20 \times$ objective lens were used to demagnify the mask features. This approach permitted successive exposures of several different patterns with accurate relative alignment of the patterns. An advantage of the projection technique is that virtually any pattern can be produced.

In the current work, a contact (one-to-one) exposure was used to expose large (a few mm on a side) regions to accommodate the inlet and outlet of the micro-model (the upper and lower rectangular regions in Fig. 1b). The micro-model was formed in the photoresist separating these regions, using the more precise projection method. To ensure a precise definition of the projection mask, a high-resolution (2500 dpi) laser printer was used on a transparent medium. By projecting through a $5 \times$ lens, this gave a resolution on the sample of 2 μm . Higher (submicron) resolutions can readily be obtained using a more powerful lens [9,10].

The procedure just described produced a pattern of open channels in a layer of photoresist. The micro-model was completed by sealing the top of the channel, and providing for inlet and outlet connections using a second glass cover slip, as shown in Fig. 1. After drilling two holes (diameter 0.5–1 mm) in the glass cover slip, it was coated with a layer of photoresist (usually AZ 1805, with a thickness of 0.5 μm) and immediately sandwiched onto the patterned substrate containing the flow pattern (Fig. 1a). The two photoresist layers formed a leak-tight bond under a light applied pressure. The integrity of this bond was readily assessed by eye; a poor bond (e.g. due to dust) resulted in pronounced interference fringes. The holes in the top glass cover slip were aligned with the inlet and outlet regions of the flow structure, allowing fluid to enter and leave.

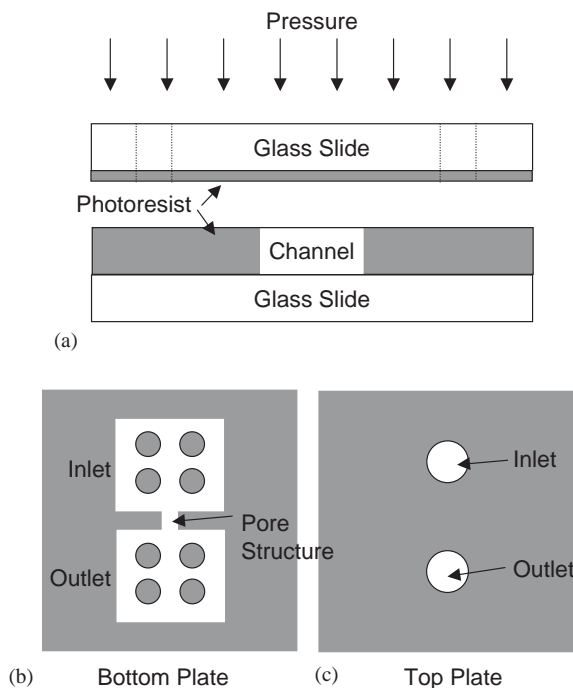


Fig. 1. Micro-model layout: (a) Side view showing bottom plate containing micro-model pattern and top plate just prior to bonding. The glass slides are cover glasses 200 μm thick. The photoresist layers are 0.5 and 1.06 μm . (b) Arrangement of inlet, outlet, and sample (channel) regions. (c) Inlet and outlet holes are drilled in the top plate. The inlet and outlet regions are approximately 3 mm \times 3 mm. The post for supporting the top plate are 300 μm in diameter. The channel width is 600 μm and the length is approximately 1.0 mm.

4. Micro-model patterns

Obtaining the geometry of the void space of a natural or induced fracture in rock is difficult [13] because rocks are opaque. To have a more direct control over the fracture properties (size, void space distribution, and correlation parameters) fracture geometries were numerically generated and used to construct the micro-model fractures. In this study, only the effect of changes

in contact area (or void space volume) was examined. The micro-model patterns were generated with a constant aperture (approximately 1.06 μm) for a range of void space areas. Simulated fractures were generated with both spatially correlated and uncorrelated void space distributions.

Numerically, each fracture was represented by an $N \times N$ array of apertures where each element of the array represents a single aperture and the entries of the array represent the fracture plane. Uncorrelated fractures were generated by taking an initially zero aperture fracture and randomly placing small squares (points) of fixed aperture within the array. Fig. 2a contains a representative image of a spatially uncorrelated fracture generated using this method. The parameters used to generate the pattern in Fig. 2a are 9400 6×6 squares inside an array size of 512×512 . Fig. 2a has a void area fraction of 0.72.

The spatially correlated aperture distributions were based on a hierarchical construction of the fracture aperture distribution known as stratified percolation [14–16]. The stratified percolation method for generating synthetic two-dimensional fractures is performed by a recursive algorithm that defines a self-similar cascade in which classical random continuum percolation is applied on successively smaller scales (tiers). The number of tiers and the number of points per tier (n) controls the spatial correlation of the void space. To start the generation, several (n) randomly positioned, equi-sized squares are chosen within the fracture array (the first tier). Within each sub-square (the second tier), n smaller squares are chosen. The sub-squares are reduced in linear size by a constant scale factor from the previous tier. This recursive process is continued until the final tier is reached. At this stage, the final small squares represent the void space. This approach leads to long-range spatial correlations because regions of non-zero aperture can only occur within regions selected throughout the hierarchy. With this algorithm it is possible to generate fractures of variable aperture [16].

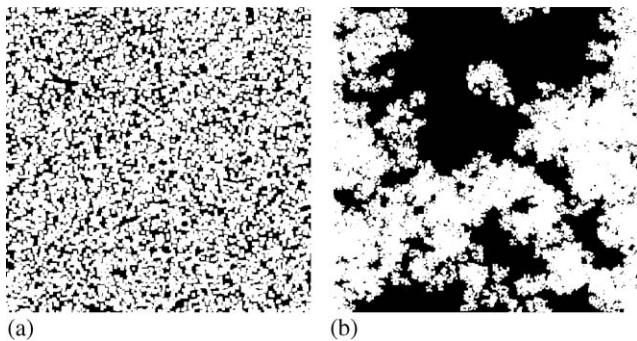


Fig. 2. Simulated fracture patterns (a) spatially uncorrelated and (b) spatially correlated. The void area fractions for (a) and (b) are 0.72 and 0.52, respectively.

Table 1

Numer of points per tier for generating uncorrelated (one tier) and spatially correlated (five tier) synthetic fractures for used in the Monte-Carlo study of the effect of contact area on fluid flow. Also given is the average void fraction and standard deviation based on two hundred simulations used to generate Figs. 6 and 7

Uncorrelated		Correlated	
Points per tier	Void area fraction	Points per tier	Void area fraction
4000	0.423 ± 0.0019	7	0.293 ± 0.015
6800	0.607 ± 0.0022	8	0.423 ± 0.028
7200	0.628 ± 0.0022	9	0.548 ± 0.037
7400	0.638 ± 0.0022	10	0.662 ± 0.046
8200	0.676 ± 0.0022	11	0.749 ± 0.049
9400	0.725 ± 0.0022	12	0.817 ± 0.049
11,000	0.779 ± 0.0022	13	0.865 ± 0.051
12,000	0.807 ± 0.0020	14	0.909 ± 0.040
13,000	0.832 ± 0.0020	15	0.930 ± 0.044
14,000	0.854 ± 0.0019	20	0.989 ± 0.014
15,000	0.873 ± 0.0018	50	1.000 ± 1 × 10 ⁻⁸
16,000	0.889 ± 0.0018		
18,000	0.916 ± 0.0016		
20,000	0.936 ± 0.0014		
30,000	0.984 ± 0.0007		
40,000	0.996 ± 0.0003		
100,000	1.000 ± 3 × 10 ⁻⁶		

However, the current study only considers fractures with a constant aperture to study the effect of changes in the amount and spatial distribution of contact area on flow. Fig. 2b shows a spatially correlated pattern generated by the stratified percolation method for a five-tier pattern generated using the following parameters: 9 points per tier, a scale factor of 2.72 between tiers, and a final square size of 4×4 within a 600×600 element array. The area fraction of void space for the pattern in Fig. 2b is 0.52.

Fractures with a range of void space areas were produced. Table 1 shows the corresponding void areas. The spatially uncorrelated (one-tier) patterns consisted of 512×512 array of ones and zeroes (representing void regions and contact area, respectively) of the numerically generated pattern. The correlated patterns (five-tier patterns) consisted of 600×600 array.

5. Flow apparatus

Flow measurements were made using the apparatus sketched in Fig. 3. Decane (J.T. Baker G143–07) was used as the fluid in the experiments. The properties of the decane are listed in Table 2. Fluid was coupled in and out of the micro-model by o-rings coupled to the holes drilled into the glass cover plate. Pressure was applied to the inlet using a syringe pump, and measured using a capacitance pressure gauge (accurate to within 2×10^{-4} atm). The flow rate was measured by observing

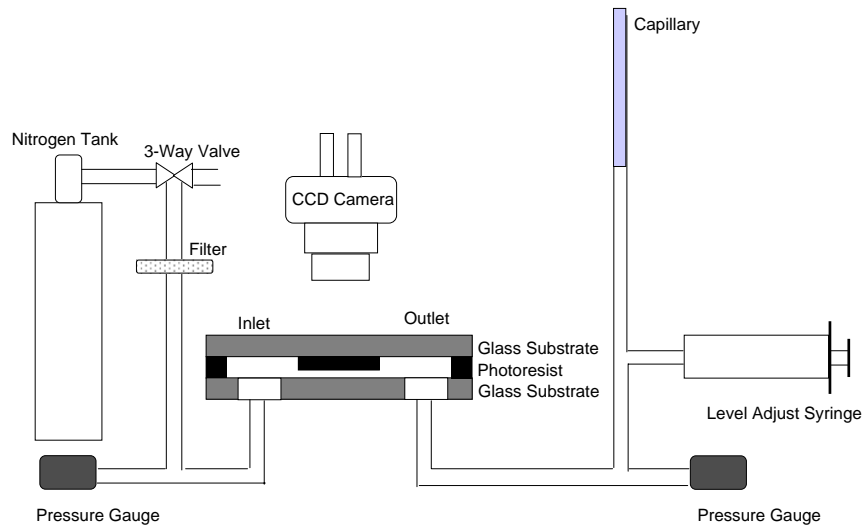


Fig. 3. Apparatus used for measurement of flow rates of decane and imaging of fluid geometry within a micro-model. The pressure sensors are piezoelectric sensors (model PX550C1 from Omega Engineering).

Table 2
Properties of decane at 24.5°C

Specific gravity	0.727 g/ml
Surface tension	24.74 mN/m
Viscosity	0.885 cp
Contact angle on glass	4.4°
Contact angle on photoresist	4.1°

and has a resolution approaching that of the microscope ($\sim 2\ \mu\text{m}$). The glass cover slips and the photoresist are transparent allowing the micro-models to be observed in either reflected or transmitted light. In addition, the optical contrast is high allowing the flow of decane to be readily observed without the need for dyes.

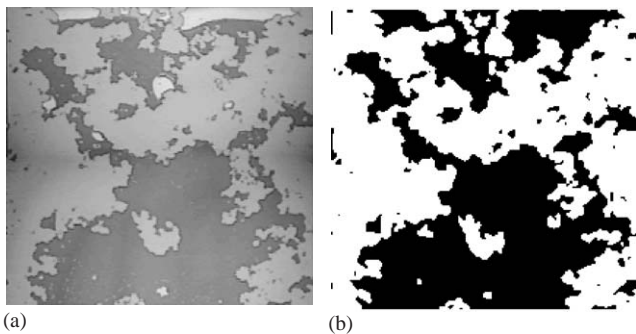


Fig. 4. (a) Captured video image of a spatially correlated micro-model generated from the pattern in Fig. 2b. (b) The thresholded image of (a).

the fluid level in an outlet capillary that had a diameter of 0.4 mm. Level changes as small as $3 \times 10^{-3}\ \text{mm/s}$ were readily measured corresponding to a flow rate of $4 \times 10^{-7}\ \text{cm}^3/\text{s}$.

In addition to measuring macroscopic properties (applied pressure difference and total flow rate) optical imaging can provide local details of fluid behavior. A CCD camera was used in conjunction with an optical microscope to observe fluid saturation in the micro-models. The image in Fig. 4a was obtained in this way,

6. Results

The data in Fig. 5 show the measured flow per unit head for the micro-model samples as a function of void area fraction for both the spatially uncorrelated and correlated micro-models. The apparatus surrounding the fracture sample has permeability associated with it that influences the measurements of the high permeability samples. The effect of the inlet and outlet regions of the flow apparatus on the measured flow rate per unit head was investigated using micro-models with a 100% void space. The average flow of three open fractures was compared with the analytic solution for flow between two parallel plates to provide an estimate of the permeability of the surrounding apparatus. For example, the analytic solution for flow between two parallel plates ($600\ \mu\text{m} \times 600\ \mu\text{m} \times 1.06\ \mu\text{m}$) gives a flow rate per unit pressure (or conductivity) of $9.776 \times 10^{-17}\ \text{m}^3/\text{Pa}$. However, three experimental measurements of the flow rate per unit pressure (or conductivity) of this case resulted in 3.318×10^{-17} , 3.998×10^{-17} , and $4.009 \times 10^{-17}\ \text{m}^3/\text{Pa}$, all substantially lower than the analytic result by an average factor of 2.6. Assuming that the measured result (k_m) is a combination of the conductivity of the sample region (k_s) and the conductivity of the surrounding regions (k_0) we have the

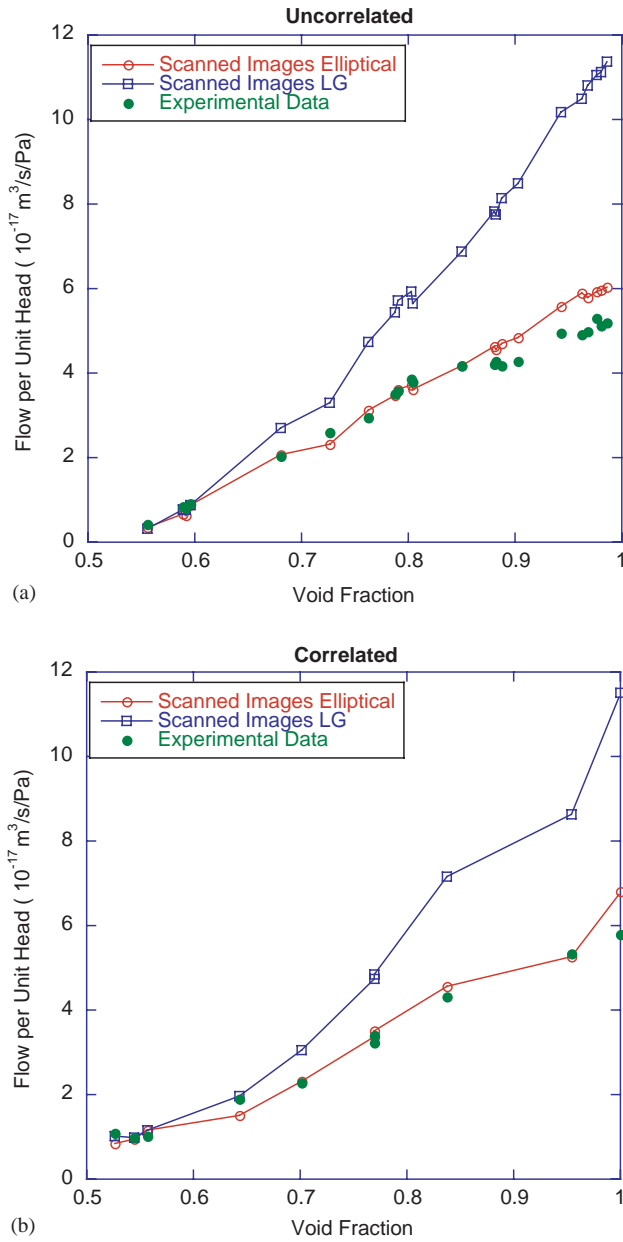


Fig. 5. Predicted flow per unit pressure from image processed data using Method I and Method II, compared with the measured flow per unit pressure data (solid circles) (a) spatially uncorrelated and (b) spatially correlated micro-models.

following:

$$k_m = \frac{k_s k_0}{k_s + k_0} \quad (1)$$

Averaging the three experimental results gives $k_m = 3.775 \times 10^{-17} \text{ m}^3/\text{s}/\text{Pa}$ and solving for k_0 in Eq. (1) gives $k_0 = 6.149 \times 10^{-17} \text{ m}^3/\text{s}/\text{Pa}$. This value was used to solve for k_s (the corrected conductivity of the sample region) for the experimental results. To account for this effect, it was assumed that the extra

conductivity of the apparatus was constant for all micro-models. The adjusted experimental results are shown in Fig. 5.

7. Analysis

The fluid flow results from the micro-model were used to validate a numerical model for simulating fluid flow through single fractures. The flow properties of the micro-model fractures were predicted numerically using a network model similar to that of Yang et al. [17,18] and Tran [19]. This method replaces the fracture with a network of pipes to approximate the flow properties of the fracture. Two algorithms were used to generate the pipe network. Method I is called the lattice-grid method and is direction-blind. The lattice-grid method creates pipes linking each aperture element of the fracture with neighboring elements, and the conductance of the pipes is calculated based upon the analytic solution for flow between two parallel plates. By considering the balance of fluid flow into and out of each aperture element, a system of linear equations is constructed for flow through the fracture. For an $N \times N$ array, this method leads to order N^2 linear equations. Many of these equations apply to regions of the fracture where further simplifications may be justified.

Method II, the second algorithm, generates a network of pipes that is not direction-blind. In Method II, the construction of the network proceeds from the inlet side of the fracture to the outlet side. Using the algorithm of Yang et al. [17,18] and Tran [19] each row of aperture elements perpendicular to the flow direction is considered in turn and contiguous regions of nonzero aperture are coalesced into single large flow elements. The flow elements generated in neighboring rows are linked by pipes with conductances given by the analytic solution for flow in an elliptical pipe. Thus, since the total number of flow elements is reduced, the total number of pipes is reduced. Flow elements in neighboring rows are joined by pipes of the maximum width (not only based on the midpoints) with the constraint that flow elements in adjacent rows were not allowed to produce flow paths which diverge by more than 45° . This corresponds to assuming that the local flow is predominantly in the same direction as the global flow. The flow results from Method II did not agree with the flow results from the lattice grid method. The calculated fluid flow results from Method II were 20–40% lowered in value than the flow predicted by the lattice grid method. The Method II calculations take significantly less time and memory to execute. Method II was typically 4–10 times faster and used 4–8 times less memory than Method I. Implicit in both network generation methods is the assumption that the fluid flow is laminar and well approximated by the analytic solutions employed locally.

Images of the micro-models captured by video (e.g., Fig. 4a) were used to provide flow boundaries for the flow simulator. Fig. 4b is the thresholded image of Fig. 4a that was used in the simulator. Numerical results obtained using the thresholded video-captured images are shown as solid circles in Fig. 5. The experimental micro-model data agree well with the numerical results from Method II (elliptical pipes) for both the correlated and uncorrelated micro-models. By simulating flow through the processed video-captured images, the micro-model behavior was reproduced to within 30–50% using Method I (lattice-grid) and to within 10–30% using Method II (elliptical pipes).

The flow rate as a function of void space fraction is not smooth for these single realizations of random patterns. Monte-Carlo simulations predict variability in flow rate for any given void space fraction. The variability in the flow properties for the correlated and uncorrelated patterns was investigated using Method II (elliptical pipes). Spatially correlated patterns (Fig. 6) exhibit a larger variability in flow than the uncorrelated patterns. A single realization of a spatially correlated void space may not be representative of all spatially correlated void space patterns because at this scale (when the correlation length is equal to the size of the sample) the fluctuations in flow dominate. However, a well-defined average flow for the ensemble is still attainable.

The flow predicted from the Monte-Carlo analysis (Fig. 6) is smaller than that measured on the micro-models (Fig. 5). While individual points in the numerically generated fractures can be resolved by the photolithographic projection (2 μm resolution) smaller features resulting from overlapping points cannot. Consequently, the video-captured image shown in Fig. 4a lacks fine structures evident in the original computer generated pattern. In particular, small blockage features are lost, and the permeability of the sample is increased.

The numerical permeabilities (flow per unit pressure) for the uncorrelated and correlated patterns exhibit percolation thresholds of $A_c = 0.6$ and 0.36 , respectively (Fig. 7). The low threshold of the correlated system is a consequence of its intrinsically small-size renormalization properties [20]. The permeability rises rapidly with increasing void area above the critical threshold (Figs. 6 and 7). Near the threshold, flow as a function of area occupancy exhibits a critical exponent given by

$$k \propto (A - A_c)^t,$$

where the flow exponent $t \approx 2$ is observed for both the correlated and uncorrelated systems. The uncorrelated systems (Fig. 7a) move into the linear effective medium regime only a little above threshold, while the correlated systems retain critical scaling up to 100% porosity (Fig. 7b).

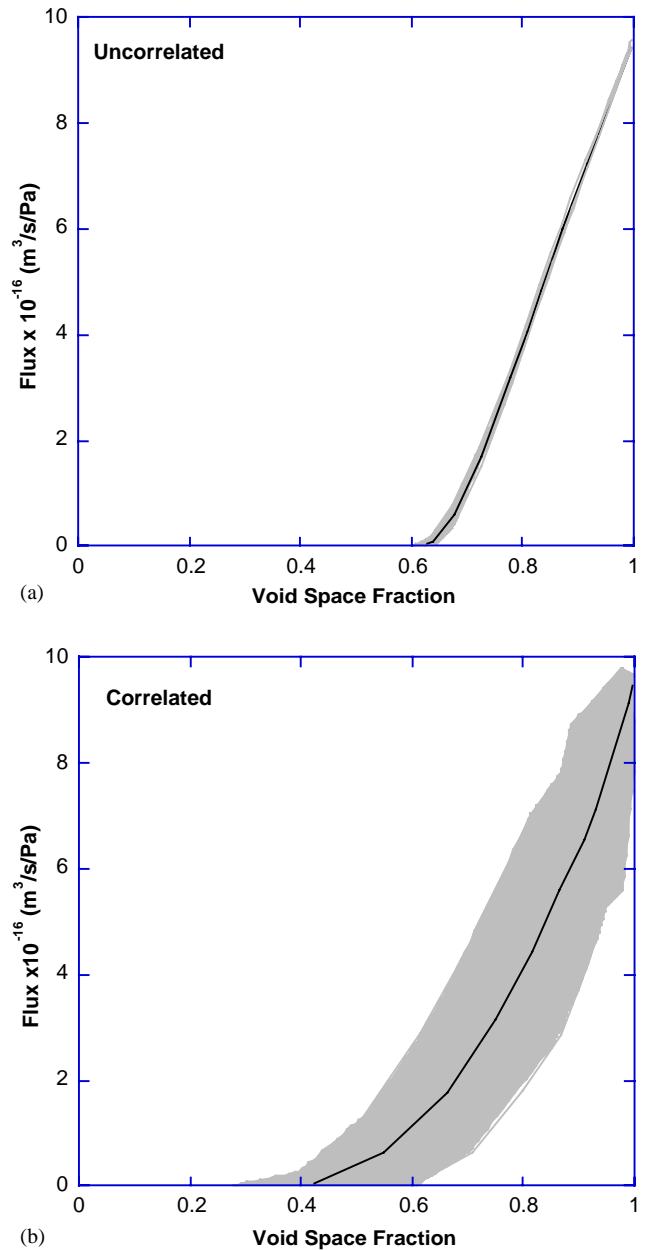


Fig. 6. Monte-Carlo results of flow per unit pressure versus saturation (void area) for (a) uncorrelated and (b) correlated patterns. The shaded regions represent the extent of one standard deviation from the mean value (black line). For each area, 200 simulations were performed.

8. Summary

Photolithography provides a means for constructing micro-models with precise, computer-generated boundaries. Because the micro-model is transparent, local flow properties can be readily observed using conventional video cameras and optical microscopes. Images of the experimental fracture geometry were used to quantify the fidelity between the original model template and the actual micro-model. These images indicated that features smaller than approximately 5 μm were not resolved

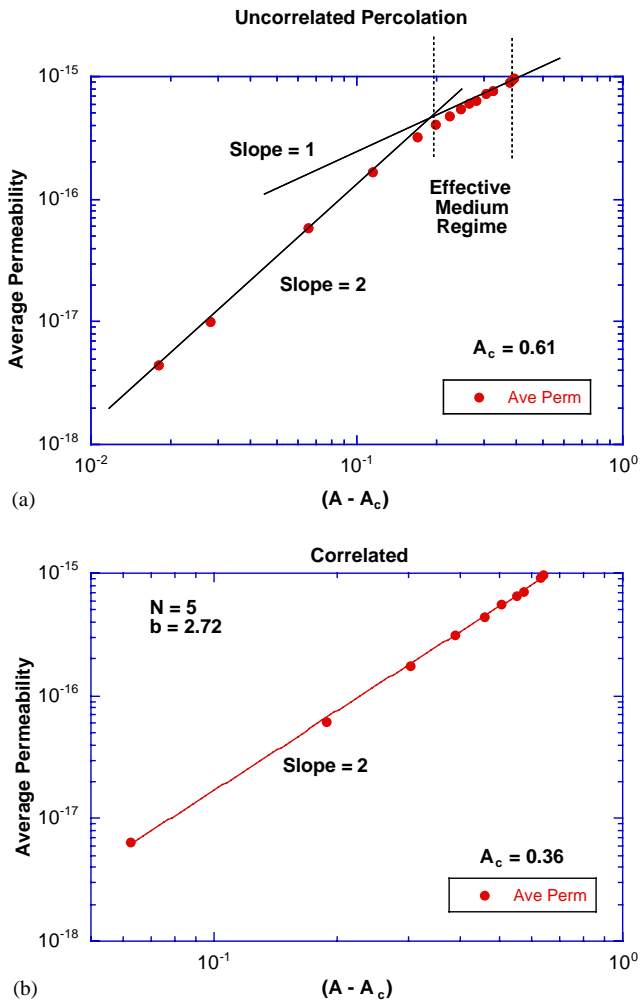


Fig. 7. Analysis of the percolation properties for the flow results from the 200 simulations for the (a) uncorrelated and (b) correlated patterns. For this figure, permeability is defined as flow per unit pressure.

in the production of the micro-models used for this study.

Two network flow models used flow boundaries obtained from images of the micro-models. The second graph-theory-based generation algorithm is much faster than simple lattice-grid and requires less memory. The lattice-grid method over-predicted the flow rates. The elliptical pipe method was found to agree well with the experimental data. However, both numerical algorithms predicted the semi-quantitative trends in flow rate observed for the micro-models.

Acknowledgements

NG would like to acknowledge G. Fiete and M. Dorbin for work on the initial experiment and NSF grant DMR-9970708. The LJP would also like to acknowledge support of this work by the Geosciences Research Program, Office of Basic Energy Sciences US Department

of Energy (DE-FG02-97ER14785 A4), by the Gas Research Institute (Contract No. 5095-260-3532) and Purdue University - University Faculty Scholar.

References

- [1] Lenormand R, Zarcone C, Sarr A. Mechanisms of the displacement of one fluid by another in a network of capillary ducts. *J Fluid Mech* 1983;135:337.
- [2] Lenormand R, Touboul E, Zarcone C. Numerical models and experiments on immiscible displacements in porous media. *J Fluid Mech* 1988;189:165.
- [3] Lenormand R. Visualization techniques in porous media. In: Hulin JF, Cazabat AM, Guyon E, Carmona F, editors. *Hydrodynamics of dispersed media*. New York: North-Holland; 1990. p. 287.
- [4] Chen J-D, Koplik J. Immiscible fluid displacement in small networks. *J Colloid Interface Sci* 1984;108:304.
- [5] Li LY, Wardlaw NC. Mechanisms of nonwetting phase trapping during imbibition at slow rates. *J Colloid Interface Sci* 1986; 109:473.
- [6] Soll WE. Development of a pore-scale model for simulating two, three phase capillary pressure-saturation relationships. PhD Thesis, Department of Civil Engineering, MIT, 1991.
- [7] Conrad SH, Wilson JL, Mason WR, Peplinski WJ. Visualization of residual organic liquid trapped in aquifers. *Water Res* 1992; 28:467.
- [8] Soll WE, Celia MA, Wilson JL. Micro-model studies of three-fluid porous media systems: pore-scale processes relating to capillary pressure-saturation relationships. *Water Res* 1993;29: 2963.
- [9] Giordano NJ, Cheng J-T. Microfluid mechanics: progress and opportunities. *J Phys: Condens Matter* 2001;13:R271–95.
- [10] Cheng J-T, Giordano NJ. Fluid flow through nanometer-scale channels. *Phys Rev E* 2002;65(3):Art. No. 031206 Part 1. MAR.
- [11] Shipley Company Inc., *Microelectronic Product Guide*, Newton, MA, 1982.
- [12] Palmer DW, Decker SK. Microscopic circuit fabrication on refractory superconducting films. *Rev Sci Instrum* 1973;44:1621.
- [13] Pyrak-Nolte LJ, Montemagno CD, Nolte DD. Volumetric imaging of aperture distributions in connected fracture networks. *Geophys Res Lett* 1997;24(18):2343–6.
- [14] Pyrak-Nolte LJ, Cook NGW, Nolte DD. Fluid percolation through single fractures. *Geophys Res Lett* 1988;15(11):1247–50.
- [15] Nolte DD, Pyrak-Nolte LJ, Cook NGW. The fractal geometry of flow paths in natural fractures in rock and the approach to percolation. *Pure Appl Geophys* 1989;131(1–2):111–38.
- [16] Nolte DD, Pyrak-Nolte LJ. Stratified continuum percolation—scaling geometry of hierarchical cascades. *Phys Rev A* 1991; 44(10):6320–33.
- [17] Yang G, Cook NGW, Myer LR. Network modelling of flow in natural fractures as a guide for efficient utilization of natural resources. *Proceedings of 30th US Symposium on Rock Mechanics*, Morgantown, West Virginia, 57–64, 1989.
- [18] Yang GM, Myer LR, Brown SR, Cook NGW. Microscopic analysis of macroscopic transport-properties of single natural fractures using graph-theory algorithms. *Geophys Res Lett* 1995;22(11):1429–32.
- [19] Tran JJ. Efficient simulation of multiphase flow in three-dimensional fracture networks. Masters thesis, Department of Computer Science and Engineering, Notre Dame University, 1998.
- [20] Nolte DD, Pyrak-Nolte LJ. Noncrossing coexistence in isotropic two-dimensional percolation. *Phys Rev E* 1997;56(4):56–60.